Efficient CC/CP Charging Control In Wireless Charging Systems For Automated Guided Vehicles

Nguyen Thi Diep[1] and Nguyen Kien Trung[2*]

[1] *Faculty of Control and Automation, Electric Power University, 235 Hoang Quoc Viet, Hanoi 100000, VietNam*
[2] *School of Electrical and Electronic Engineering, Hanoi University of Science and Technology, 01 Dai Co Viet, Hanoi 100000, VietNam*
[*] *Corresponding author. E-mail: trung.nguyenkien1@hust.edu.vn*

Received: Jan. 10, 2026; Accepted: Jul. 10, 2026

Wireless power transfer has emerged as an attractive solution for charging automated guided vehicles (AGVs) in modern industrial environments. In practice, many AGVs adopt *opportunity charging*, where vehicles are recharged during short idle periods along their operating routes. Under such conditions, constant-current (CC) charging ensures battery safety at low states of charge, while constant-power (CP) charging maximizes energy delivery within limited charging time. Consequently, CC/CP charging control is particularly suitable for wireless AGV opportunity charging systems. This paper proposes an efficiency-oriented CC/CP charging control strategy based on an optimized dual-side LCC compensation topology and a secondary-side control scheme using a semi-active rectifier with pulse-density modulation (PDM). The proposed approach integrates the optimized dual-side LCC circuit with the semi-active rectifier and PDM control to enable efficient CC/CP regulation with a simple control structure while maintaining high power transfer efficiency over a wide load range. Simulation and experimental results verify the effectiveness of the proposed approach, demonstrating accurate CC/CP regulation, fast dynamic response, and robust operation under wide load variations, with peak efficiencies of 96.6% in simulation and 93.1% in the experimental prototype.

Keywords: Automated guided vehicle; Wireless charging; Dual-side LCC compensation; CC/CP charging control; Opportunity charging

© The Author('s). This is an open-access article distributed under the terms of the Creative Commons Attribution License (CC BY 4.0), which permits unrestricted use, distribution, and reproduction in any medium, provided the original author and source are cited.

http://dx.doi.org/10.6180/jase.202611_34.061

1. Introduction

Automated Guided Vehicles (AGVs) have been widely deployed in modern industrial environments such as smart factories, warehouses, and logistics centers to enhance productivity, operational flexibility, and safety. As AGVs operate continuously and autonomously, reliable and efficient battery charging is critical. Compared with conventional plug-in charging, wireless power transfer (WPT) eliminates physical electrical contacts, thereby reducing mechanical wear and maintenance while enabling fully autonomous charging [1–6]. Consequently, WPT converter topologies and charging control strategies have been extensively studied for electric transportation applications [7].

Despite these advantages, achieving high-efficiency WPT for AGVs remains challenging because battery charging requires both CC and CP modes. Lithium-ion batteries operate in CC mode at low states of charge (SoC) and CP mode at higher SoC, particularly in opportunity charging. As the SoC increases, the equivalent load impedance changes, increasing reactive power and reducing transfer efficiency even under well-aligned conditions. Therefore, maintaining high efficiency over a wide load range across both charging stages is essential for practical AGV wireless charging systems.

Resonant compensation design plays a key role in addressing this challenge. Among various topologies, dual-side LCC compensation has attracted considerable attention because of its high power transfer efficiency, low sensitivity to load and coupling variations, and soft-switching capability [8–14], making it well suited to AGV wireless charging systems. However, existing designs are generally optimized for nominal operating points and fail to maintain optimal efficiency over the wide load range required for CC/CP charging [15–18]. As the battery load deviates from the design point, increased reactive power circulation reduces transfer efficiency. To overcome this limitation, this paper proposes an efficiency-optimized dual-side LCC compensation design that maintains high efficiency throughout the CC and CP charging stages.

Various charging control strategies have been developed for WPT systems. LCC-based compensation can inherently achieve CC or CV characteristics through parameter tuning [17–19]; however, its regulation accuracy and efficiency deteriorate under the wide load variations of multi-stage battery charging [20]. To improve controllability, secondary-side control using active or semi-active rectifiers has been proposed for CC/CV regulation and efficiency optimization [21–23], whereas primary-side-only control reduces hardware complexity but offers limited robustness against simultaneous load and coupling variations [24, 25]. More recently, CP regulation has been introduced to improve power control and transfer efficiency [26, 27]; however, existing solutions often increase control complexity or provide limited flexibility during CC/CP transition. Therefore, a simple and robust secondary-side strategy that enables accurate CC/CP regulation, smooth CC/CP transition, and high efficiency over a wide load range for AGV opportunity charging remains lacking.

To address these challenges, this paper proposes an efficient CC/CP charging control strategy for wireless AGV charging systems. The proposed approach combines an efficiency-optimized dual-side LCC compensation topology with a secondary-side semi-active rectifier using pulse-density modulation (PDM) to achieve accurate CC/CP regulation, smooth mode transition, and high efficiency over a wide load range. The main contributions of this paper are summarized as follows:

1. An efficiency-oriented CC/CP charging control strategy is proposed for wireless AGV charging systems operating under opportunity charging conditions, where wide load variations occur during multi-stage battery charging.

2. An efficiency-optimized dual-side LCC compensation topology is developed to maintain high power transfer efficiency across the wide load range encountered during both CC and CP charging stages.

3. A simple secondary-side control scheme based on a semi-active rectifier and PDM is designed to achieve accurate CC/CP regulation with a well-damped CC/CP transition while reducing control complexity.

The remainder of this paper is organized as follows. Section II presents the proposed system and efficiency-optimized dual-side LCC design. Section III describes the semi-active rectifier and CC/CP charging control strategy. Section IV provides simulation and experimental validation. Finally, Section V concludes the paper.

2. Methods

2.1. Proposed System Structure

Fig. 1 shows the proposed system, which consists of a high-frequency inverter, a dual-side LCC compensation network, and a secondary-side semi-active rectifier (SAR). The primary-side LCC network generates the high-frequency excitation current, while the secondary-side network enables stable and efficient power transfer under varying coupling conditions.

On the secondary side, a SAR is adopted to reduce conduction losses compared with fully active rectification while maintaining sufficient regulation capability. To achieve a regulated charging operation, a dedicated CC/CP Charging Control Block is incorporated. This control block receives the current and power reference signals, together with the measured load current and power, and generates appropriate gate-driving signals for the SAR.

In this study, the battery load is represented by an equivalent DC resistance, R_{Load}. From the DC output side of the semi-active rectifier, R_{Load} emulates the battery voltage–current characteristic during charging and is used to evaluate the proposed CC/CP charging strategy. Although this simplified model does not fully capture the nonlinear behavior of a practical lithium-ion battery, such as SoC dependence, internal resistance variation, and electrochemical dynamics, it provides a well-defined and repeatable operating condition for assessing the charger-side control performance. Therefore, the resistive-load model provides a practical and repeatable means of evaluating the proposed CC/CP charging control strategy under well-defined operating conditions. However, it does not reproduce the complete electrochemical behavior of a practical lithium-ion battery.

A zero-crossing detector (ZCD) monitors the secondary-side resonant current before the SAR, as shown in

Fig. 1. The detected zero-crossing instant synchronizes the sigma–delta-based PDM controller, ensuring proper alignment between the SAR switching actions and the resonant current. This improves control stability while reducing switching losses.

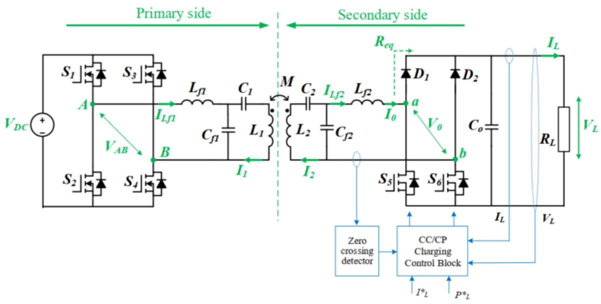

Fig. 1. Structure of the proposed wireless charging system for AGVs

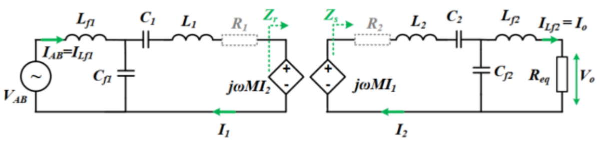

Fig. 2. Equivalent circuit diagram of the compensation circuit

2.2. Dual-Side LCC Compensation Design for Efficiency Optimization

As shown in Fig. 2, V_{AB} is the fundamental inverter voltage; I_1 and I_2 are the transmitter and receiver currents; and M is the mutual inductance; $L_{1,2}$, $L_{f1,f2}$, $C_{1,2}$, and $C_{f1,f2}$ represent the compensation components; $R_{1,2}$ are the coil resistances; and R_{eq}, I_o, and V_o denote the equivalent AC load resistance, output current, and output voltage, respectively. Applying Kirchhoff's second law to the primary- and secondary-side voltage loops yields:

$$V_{AB} = \left(j\omega L_{f1} + \frac{1}{j\omega C_{f1}}\right) I_{Lf1} - \frac{1}{j\omega C_{f1}} I_1, \tag{1}$$

$$j\omega M I_1 = \left(j\omega L_2 + \frac{1}{j\omega C_2} + \frac{1}{j\omega C_{f2}}\right) I_2 - \frac{1}{j\omega C_{f2}} I_o, \tag{2}$$

The resonance conditions of the dual-sided LCC compensation circuit are given by

$$j\omega L_{f1} + \frac{1}{j\omega C_{f1}} = 0, \tag{3}$$

$$j\omega L_2 + \frac{1}{j\omega C_2} + \frac{1}{j\omega C_{f2}} = 0, \tag{4}$$

Under these conditions, the output current is expressed as

$$I_0 = -j\omega^3 C_{f1} C_{f2} M V_{\mathrm{AB}} = \frac{M V_{\mathrm{AB}}}{j\omega L_{f1} L_{f2}}, \tag{5}$$

The primary-side inverter operates with square-wave modulation, yielding

$$V_{AB} = \frac{2\sqrt{2}}{\pi} V_{\mathrm{DC}} \tag{6}$$

From (5) and (6), the output current I_0 can be derived as

$$I_0 = \frac{2\sqrt{2}\, M\, V_{\mathrm{DC}}}{j\pi\omega L_{f1} L_{f2}} \tag{7}$$

Zero-phase-angle (ZPA) operation is achieved when the input impedance is purely resistive, which requires

$$j\omega L_{f2} + \frac{1}{j\omega C_{f2}} = 0, \tag{8}$$

$$j\omega L_1 + \frac{1}{j\omega C_1} + \frac{1}{j\omega C_{f1}} = 0 \tag{9}$$

Equation (7) indicates that the dual-side LCC compensation exhibits a current-source characteristic, making it suitable for AGV opportunity charging. The design is constrained by the five equations (3), (4), (8), (9), and (7), which determine six compensation parameters (L_{f1}, C_{f1}, C_1, L_{f2}, C_{f2}, and C_2). Therefore, one design degree of freedom remains for efficiency optimization. Considering the transmitter and receiver coil resistances R_1 and R_2, respectively, the overall transfer efficiency is given by

$$\eta_{\text{transfer}} = \eta_{\text{primary}} \times \eta_{\text{secondary}}. \tag{10}$$

The secondary-side efficiency is given by

$$\eta_{\text{secondary}} = \frac{R_{\text{eq}}}{R_{\text{eq}} + R_2 \left(\frac{I_2}{I_0}\right)^2}, \tag{11}$$

where the current ratio is derived from

$$(j\omega L_{f2} + \tfrac{1}{j\omega C_{f2}} + R_{eq}) I_0 - \tfrac{1}{j\omega C_{f2}} I_2 = 0, \tag{12}$$

leading to

$$\left|\frac{I_2}{I_0}\right|^2 = \left(\frac{R_{eq}}{\omega L_{f2}}\right)^2. \tag{13}$$

Thus,

$$\eta_{\text{secondary}} = \frac{1}{1 + \dfrac{R_2 R_{\text{eq}}}{\omega^2 L_{f2}^2}}. \tag{14}$$

The reflected impedance on the primary side is

$$Z_r = \frac{(\omega M)^2}{Z_s}, \tag{15}$$

where

$$Z_s = R_2 + \frac{\omega^2 L_{f2}^2}{R_{\text{eq}}}. \tag{16}$$

Accordingly, the primary-side efficiency becomes

$$\eta_{\text{primary}} = \frac{(\omega M)^2}{(\omega M)^2 + R_1\left(R_2 + \frac{\omega^2 L_{f2}^2}{R_{eq}}\right)}. \tag{17}$$

Substituting (14) and (17) into (10) yields

$$\eta_{\text{transfer}} = (\omega M)^2 \omega^2 L_{f2}^2 \times \left[\frac{\omega^4 R_1}{R_{\text{eq}}} L_{f2}^4 + \omega^2\left(2R_1R_2 + (\omega M)^2\right) L_{f2}^2 + \left(R_1R_2 + (\omega M)^2\right) R_2 R_{\text{eq}}\right]^{-1} \tag{18}$$

To simplify the transfer efficiency expression, a variable substitution and several coefficient definitions are introduced as

$$X \triangleq L_{f2}^2, \qquad b_1 = (\omega M)^2\omega^2, \qquad b_2 = \frac{\omega^4 R_1}{R_{eq}},$$
$$b_3 = \omega^2\left(2R_1R_2 + (\omega M)^2\right), \qquad b_4 = \left(R_1R_2 + (\omega M)^2\right) R_2 R_{eq}. \tag{19}$$

Substituting these definitions into the transfer efficiency expression in (18), it can be rewritten in the compact form

$$\eta_{\text{transfer}}(X) = \frac{b_1 X}{b_2 X^2 + b_3 X + b_4}. \tag{20}$$

To determine the maximum transfer efficiency, the derivative of $\eta_{\text{transfer}}(X)$ with respect to X is set to zero, i.e.,

$$\frac{d\,\eta_{\text{transfer}}(X)}{dX} = 0. \tag{21}$$

Solving this condition yields the optimal solution

$$X_{\text{opt}} = \sqrt{\frac{b_4}{b_2}}. \tag{22}$$

Since $X = L_{f2}^2$, the optimal value of the secondary compensation inductance is obtained as

$$L_{f2,\text{opt}} = \sqrt[4]{\frac{\left(R_1R_2 + (\omega M)^2\right)\, R_2\, R_{eq}^2}{\omega^4 R_1}}. \tag{23}$$

Substituting the optimal condition into the efficiency expression gives the corresponding maximum transfer efficiency

$$\eta_{\max} = \left(\frac{\omega M}{\sqrt{R_1R_2} + \sqrt{R_1R_2 + (\omega M)^2}}\right)^2. \tag{24}$$

In AGV wireless charging systems, the transmitter and receiver coils are typically fixed and well aligned. Therefore, the parameters R_1, R_2, ω, and M can be considered constant. Under these conditions, the optimal inductance $L_{f2,\text{opt}}$ mainly depends on the equivalent load resistance R_{eq}.

However, since R_{eq} varies with the load, the exact value of $L_{f2,\text{opt}}$ also changes. To maintain high efficiency over the entire load range while keeping the circuit design practical, the secondary compensation inductance L_{f2} is selected as a fraction of the secondary coil inductance L_2:

$$L_{f2} = cL_2, \qquad 0 < c < 1. \tag{25}$$

where c is the design coefficient used for efficiency optimization over the target load range.

Based on the AGV charging specifications ($I_{\text{CC}} = 20$ A and $P_{\text{CP}} = 1.6$ kW), the battery equivalent resistance varies from 2–4 Ω during CC charging and 4–6 Ω during CP charging. Referred to the AC side, this corresponds to an equivalent load resistance of $R_{\text{eq}} = 1.62$–$4.86\,\Omega$, which is adopted for the efficiency analysis. Therefore, the coefficient analysis is conducted by sweeping R_{eq} within this range. Fig. 3(a) shows that the transfer efficiency reaches its maximum around $c = 0.2$, where the efficiency curves converge to approximately 97%. Accordingly, the optimal coefficient is selected as $c_{\text{opt}} = 0.2$.

With c_{opt} determined, L_{f2}, L_{f1}, and the compensation capacitances are calculated from (7) and the resonance conditions. The complete system parameters are listed in Table 1. An operating frequency of 40 kHz is adopted for the proposed AGV wireless charging system.

To evaluate the robustness of the optimized design, the coupling coefficient is varied from 70% to 100% of its nominal value while maintaining $c_{\text{opt}} = 0.2$. As shown in Fig. 3(b), the transfer efficiency decreases gradually with decreasing coupling coefficient because of the reduced mutual inductance, but remains above 94.5% over the entire load range. These results demonstrate that the proposed design is robust against moderate coupling variations caused by coil misalignment or air-gap changes during AGV docking.

Although explicit misalignment analysis is beyond the scope of this study, the coupling-coefficient variation provides an indirect evaluation of moderate coil misalignment. Therefore, the proposed design is expected to maintain satisfactory performance under moderate misalignment. A comprehensive experimental and analytical investigation of lateral and angular misalignment will be conducted in future work.

Table 1. Main parameters of the system

Parameter	Symbol	Value
DC input voltage	V_{DC}	310 V
Operating frequency	f	40 kHz
Maximum output charging current	I_L	20 A
Self-inductance of transmitter/receiver coils	L_1, L_2	112.5 μH
Internal resistance of transmitter/receiver coils	R_1, R_2	0.15 Ω
Magnetic coupling coefficient	k	0.39
Mutual inductance	M	43.875 μH
Transmitter compensation inductance	L_{f1}	108.31 μH
Transmitter lower-branch compensation capacitor	C_{f1}	0.146 μF
Transmitter upper-branch compensation capacitor	C_1	3.746 μF
Receiver compensation inductance	L_{f2}	22.5 μH
Receiver lower-branch compensation capacitor	C_{f2}	0.703 μF
Receiver upper-branch compensation capacitor	C_2	0.176 μF
Equivalent load resistance	R_{eq}	1.62 Ω – 4.86 Ω
Output filter capacitor	C_0	470 μF

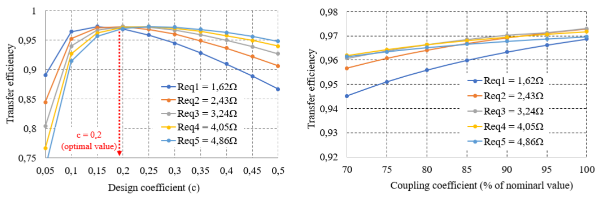

(a) Transfer efficiency versus design coefficient c

(b) Transfer efficiency versus coupling coefficient with c = 0.2

Fig. 3. Efficiency analysis of the optimized inductance design

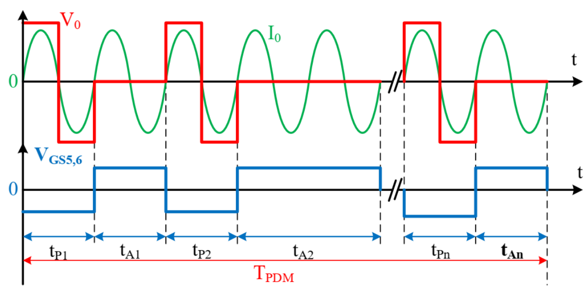

Fig. 5. The voltage and current waveforms of the PDM method

2.3. Theoretical analysis of semi-active rectifier control

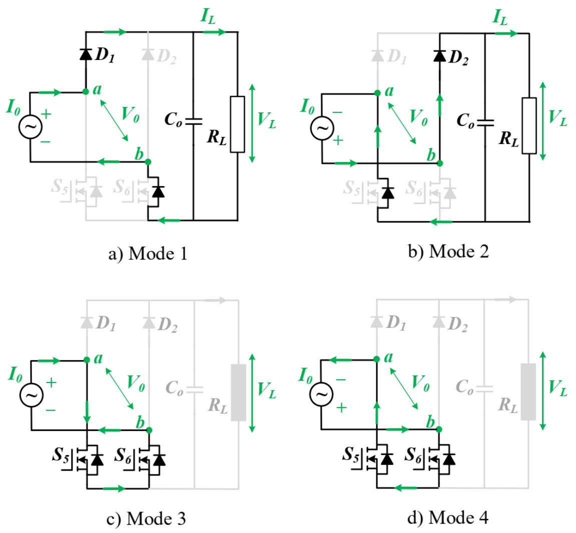

Fig. 4. Operating modes of the semi-active rectifier with pulse density modulation control

The dual-side LCC compensation inherently provides a current-source characteristic, while the secondary-side SAR is controlled by PDM for AGV charging regulation. The SAR operates in four modes, as illustrated in Fig. 4. With S_5 and S_6 turned off, it operates as a diode rectifier. When they are turned on, the rectifier input is short-circuited, and the load is temporarily supplied by the output capacitor C_0, which smooths the output voltage and suppresses the low-frequency ripple caused by PDM.

The capacitor C_0 determines the trade-off between output ripple and transient response. A larger capacitance reduces ripple but slows the transient response, whereas a smaller capacitance improves the dynamic response at the expense of higher ripple. Therefore, $C_0 = 470\,\mu$F is selected as a compromise. The corresponding waveforms are shown in Fig. 5.

The PDM duty ratio d is the ratio of the passive-state duration to the PDM period.

$$d = \frac{\sum t_{Pi}}{\sum t_{Pi} + \sum t_{Ai}} = \frac{\sum t_{Pi}}{t_{PDM}}, \tag{26}$$

where t_{Pi} and t_{Ai} denote the time intervals during which the MOSFETs operate in the passive and active states, respectively, and t_{PDM} is the PDM modulation period.

Under PDM operation, the RMS input voltage and current of the SAR are given by

$$V_0 = \frac{2\sqrt{2}}{\pi} V_L d, \tag{27}$$

$$I_0 = \frac{2\sqrt{2}}{\pi R_L} V_L d. \tag{28}$$

Based on power balance $V_0 I_0 = V_L I_L$,

$$I_L = \frac{2\sqrt{2}}{\pi} I_0 d, \tag{29}$$

$$R_{eq} = \frac{8}{\pi^2} R_L d^2. \tag{30}$$

Accordingly, the average charging power is

$$P_L = I_0^2 R_{eq}. \tag{31}$$

Since the dual-side LCC compensation exhibits an inherent current-source characteristic, I_0 in (7) is determined by the system parameters and remains load-independent under aligned conditions. Thus, the charging current I_L is directly regulated by the PDM factor d, enabling CC charging without current feedback. Moreover, since P_L is proportional to R_{eq} for constant I_0, adaptive adjustment of d achieves CP charging under varying loads.

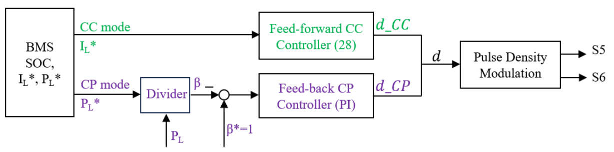

Fig. 6. Constant-current, constant-power control strategy

2.4. Control Strategy of CC/CP Charging Process

Fig. 6 illustrates the proposed CC/CP charging strategy. The charging process consists of CC and CP modes for fast charging at low SoC and efficient operation at high SoC.

In the CC mode, the inherent current-source characteristic of the dual-side LCC compensation allows the PDM factor d to be directly calculated from the reference current I_L^* using (7) and (29). Therefore, accurate CC regulation is achieved without current feedback, reducing control complexity and improving reliability.

As the battery voltage increases, the controller switches to CP mode to limit the charging power. The charging power is calculated from the measured secondary-side voltage and current as

$$P_L = V_L I_L. \tag{32}$$

The calculated power is fed back for CP regulation, maintaining constant charging power under load variations.

The charging power is normalized by the reference power P_L^* to obtain

$$\beta = \frac{P_L}{P_L^*}. \tag{33}$$

The normalized power coefficient β is used as the CP feedback signal.

The small-signal transfer function from the PDM factor d to the charging power is identified using the MATLAB Identification Toolbox as

$$G_{d\beta}(s) = \frac{21.55s + 3.452 \times 10^5}{s^2 + 1267s + 3.469 \times 10^5}. \tag{34}$$

A proportional–integral (PI) controller is designed as

$$G_{\text{PI}}(s) = 2 + \frac{580}{s}. \tag{35}$$

The PI controller regulates the power error $(\beta - 1)$ to generate the PDM factor d, thereby adjusting the equivalent load resistance and maintaining constant charging power despite load variations.

The controller switches from CC to CP when

$$P_L = I_L^* V_L \geq P_L^*. \tag{36}$$

Thereafter, the charging power is maintained at P_L^* while the charging current naturally decreases as the battery voltage increases. Charging terminates when the current falls below a predefined cutoff value or the battery SoC reaches its upper limit.

Owing to the inherent current-source characteristic of the WPT system, the proposed CP operation exhibits CV-like behavior without an explicit constant-voltage stage, ensuring stable power regulation over a wide load range.

3. Results and discussion

3.1. Simulation Results

The proposed system was modeled in MATLAB/Simulink using the parameters in Table 1. Simulations were conducted to validate CC charging, CP regulation, and CC–CP transition under wide load variations.

In Scenario 1, CC charging was evaluated with a reference current of 20 A while varying the load resistance R_L from 1 Ω to 4 Ω. As shown in Fig. 7(a), the charging current settles within 0.01 s at an average value of 19.53 A, corresponding to a deviation of 2.35%, with a ripple of only 0.46 A (0.15%). Fig. 7(b) shows the response to a reference step from 10 A to 20 A under a 2 Ω load. In both cases, the steady-state error remains below 5%, with current ripple of 1.6% at 10 A and 0.15% at 20 A, confirming accurate CC regulation through direct PDM control.

Fig. 8 shows the CP charging performance with a reference power of 1500 W. Under a fixed load of 4 Ω, the

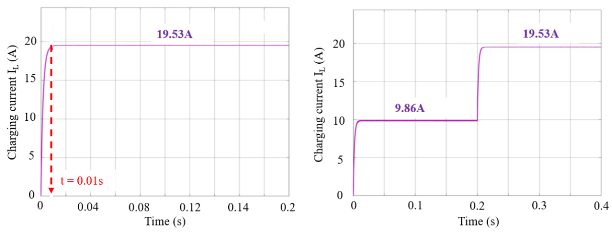

(a) Charging current at 20 A. **(b)** Charging current from 10 A to 20 A

Fig. 7. Charging current response under constant-current control

output power is regulated at approximately 1490 W with a steady-state error of 4% (Fig. 8(a)). When the load resistance varies from 4 Ω to 6 Ω in steps of 0.5 Ω every 0.2 s (Fig. 8(b)), the power regulation remains stable, achieving a settling time of about 0.017 s despite abrupt load changes. These results demonstrate the robustness of the proposed CP control strategy.

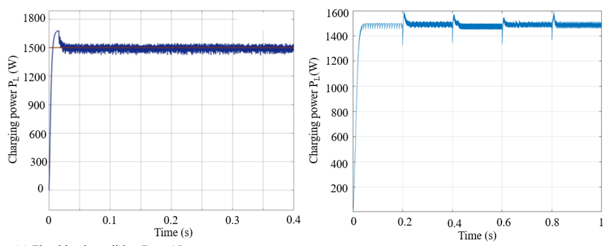

(a) Fixed load condition R_L = 4Ω. **(b)** Load variation from 4 Ω to 6 Ω.

Fig. 8. Charging power response under constant-power control

The CC–CP transition is illustrated in Fig. 9. The load resistance R_L is increased from 3.5 Ω in steps of 0.5 Ω every 0.05 s. As shown in Fig. 9(a), the charging current is regulated around the CC reference before the transition and decreases gradually once the load exceeds the CC operating range. The operating mode switches from CC to CP at approximately $t = 0.15$ s.

Fig. 9(b) shows the corresponding charging power. During the transition, the charging power exhibits an overshoot of approximately 10% above the 1500 W reference and settles within 10 ms without sustained oscillation. A small steady-state ripple remains because of the discrete PDM operation; however, the average charging power stays close to the reference value. These results demonstrate a well-damped transition and stable CC/CP regulation.

Fig. 10(a) shows the zoomed-in waveforms of the primary inverter switch S_1 at the minimum and maximum loads. Despite the significant variation in switch current, the drain-to-source voltage falls to nearly zero before turn-on in both cases, confirming ZVS over the entire load range

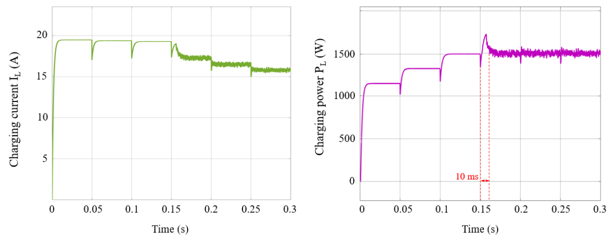

(a) Charging current response. **(b)** Charging power response.

Fig. 9. Charging current and power responses under combined CC/CP control

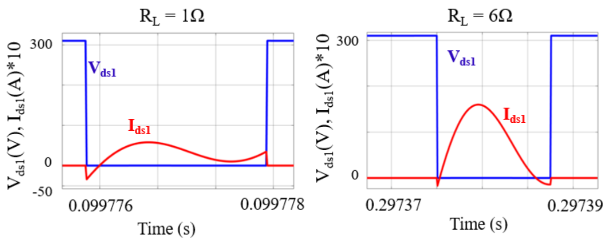

(a) Primary inverter switch S_1.

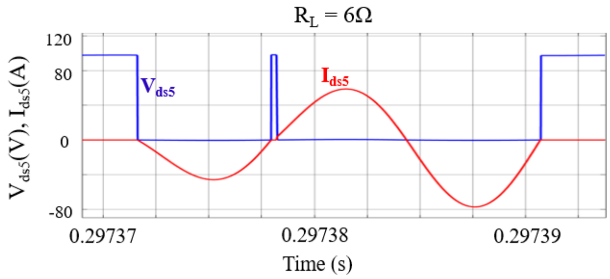

(b) SAR switch S_5 (worst-case).

Fig. 10. Voltage and current waveforms of the primary inverter and SAR switches.

(R_L = 1–6 Ω) in both CC and CP modes.

Fig. 10(b) shows the voltage and current waveforms of the SAR switch S_5 under the worst-case condition (R_L = 6 Ω). The drain-to-source voltage is nearly zero at turn-on, indicating near-ZVS. The maximum drain-to-source voltage and peak drain current are approximately 100 V and 78 A, respectively.

3.2. Experimental Results

An experimental prototype was built to validate the proposed system, as shown in Fig. 11. The system parameters are listed in Table 1. A controllable resistive load was used to emulate the battery under repeatable test conditions. The proposed SAR–PDM strategy is implemented entirely on the secondary side, with the controller updated at the PDM frequency of 2.5 kHz ($T_{PDM} = 400$ μs, corresponding to 16 switching cycles at 40 kHz).

Although an actual AGV lithium-ion battery exhibits more complex dynamics than the adopted resistive-load model, the proposed CC/CP charging strategy is expected to exhibit similar performance in practice. As the battery SoC increases, the terminal voltage rises, causing the equivalent load seen by the WPT system to vary continuously and the charging process to naturally transition from CC to CP. Since the controller regulates the charging current and output power using measured output quantities, the battery dynamics mainly shift the operating point without changing the operating principle. Therefore, smooth CC/CP transition is expected during practical battery charging.

The TX and RX coils are identical circular Litz-wire coils with ferrite cores. Each coil has an outer diameter of 17 cm, an inner diameter of 5.5 cm, 26 turns, and a wire diameter of 2 mm. Eight ferrite bars (5.5 × 1.8 × 0.5 cm) are placed beneath each coil to enhance magnetic coupling, with an air gap of 40 mm.

The primary inverter employs four SPW20N60C3 MOSFETs, while the SAR uses two DSA90C200HB diodes and two IXFH120N20P MOSFETs. As verified by the stress analysis in Fig. 10, their voltage and current ratings (200 V and 120 A, respectively) provide sufficient design margin for reliable operation.

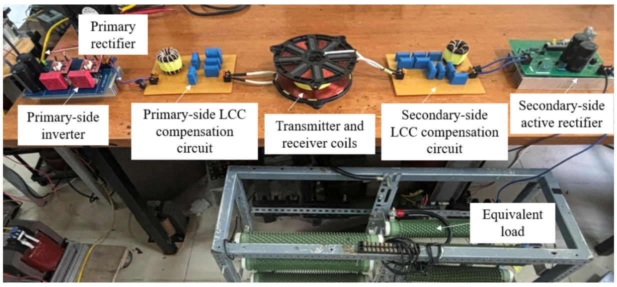

Fig. 11. Experimental model

Fig. 12 shows the measured inverter output voltage and current, as well as the voltage across the TX coil. As shown in Fig. 12(a), the full-bridge inverter generates a square-wave voltage, while the inverter current is shaped by the resonant network. Due to the filtering effect of the resonant compensation circuit, the voltage across the TX coil in Fig. 12(b) becomes nearly sinusoidal. The inverter operates at the designed switching frequency of 40 kHz, and ZVS is achieved, validating the effectiveness of the compensation circuit.

Fig. 13 presents the experimental waveforms on the receiving side. As shown in Fig. 13(a), the voltage across the RX coil is also approximately sinusoidal due to the resonant operation of the wireless power transfer system. Fig. 13(b) shows the input voltage and current of the semi-active rectifier, where the voltage follows the rectified waveform while the current remains nearly sinusoidal. These results confirm stable power transfer and proper operation of the rectifier under the proposed control strategy.

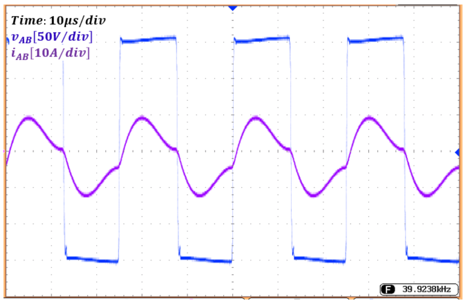

(a) Inverter output voltage and current.

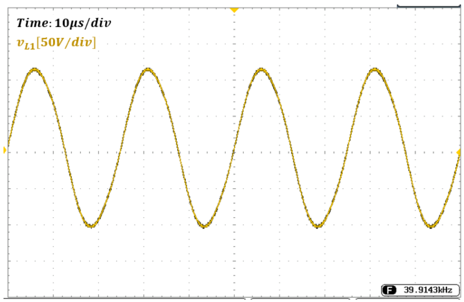

(b) Voltage across the transmitting coil.

Fig. 12. Experimental waveforms of inverter output and transmitting coil.

The CC charging performance is experimentally validated in Fig. 14 at $R_L = 3\ \Omega$. Fig. 14(a) shows that the rectifier input voltage and current remain in phase at $d = 0.5$, indicating an approximately resistive equivalent input impedance. Fig. 14(b) confirms stable current regulation at 10 A, in close agreement with simulation results.

Fig. 15 shows the measured load voltage and current during CP charging with a reference power of 1500 W at $R_L = 5.2\ \Omega$. The average voltage and current are approximately 88 V and 16.8 A, respectively, resulting in a charging power of about 1.48 kW with a deviation of 1.4%, which confirms accurate CP regulation.

The system efficiency characteristics are illustrated in Fig. 16. Over the entire regulation range, the proposed system maintains high power transfer efficiency. In the CC region ($R_L = 1$–$4\ \Omega$), both simulation and experimental efficiencies increase with load and reach peak values of approximately 96.6% and 93.1%, respectively. As the system transitions into the CP region ($R_L = 4$–$6\ \Omega$), a slight efficiency degradation is observed due to reduced power transfer; nevertheless, the efficiency remains at a high level.

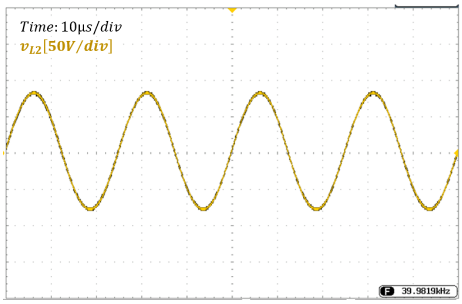

(a) Voltage waveform across the receiving coil.

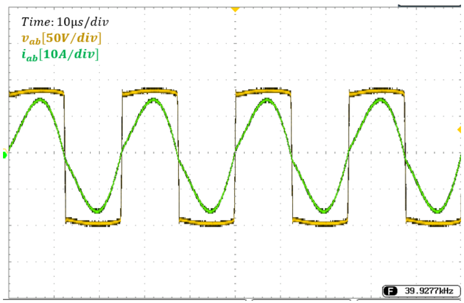

(b) Active rectifier input voltage and current.

Fig. 13. Experimental waveforms at the receiving coil and rectifier input.

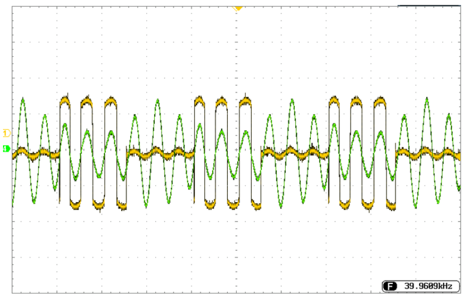

(a) Input voltage and current of the rectifier under CC mode.

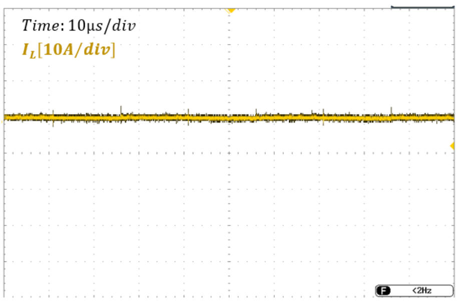

(b) Charging current regulated at 10 A.

Fig. 14. Experimental waveforms under CC charging operation.

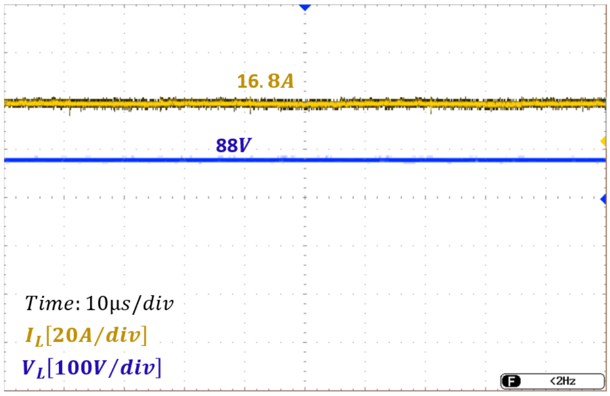

Fig. 15. Measured load voltage and current during CP charging

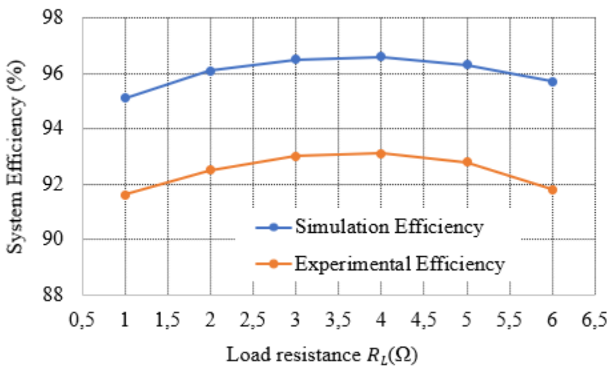

Fig. 16. System efficiency characteristics

Overall, the average efficiency exceeds 96% in simulation and 92.4% in experiment across the full operating range, demonstrating the effectiveness of the proposed system and good agreement between theoretical analysis and experimental results.

The peak efficiency difference between simulation and experiment is approximately 3.5%. This efficiency gap is mainly caused by practical non-ideal losses, including semiconductor switching and conduction losses, parasitic resistances of passive components and interconnections, and thermal effects during operation, which are not fully represented in the simulation model.

4. Conclusions

This paper has presented an efficient CC/CP charging control in wireless charging systems for AGVs, based on an optimized dual-side LCC compensation circuit and a secondary-side control strategy using a semi-active rectifier and pulse-density modulation. The proposed design maintains high transfer efficiency over the wide load range encountered during CC and CP charging, while the current-source characteristic of the LCC circuit enables simple feedforward CC control and PI-based CP regulation with stable CC–CP transition. Both simulation and experimental results verify accurate CC/CP regulation, fast dynamic response, and robust performance under load variation, achieving peak efficiencies of 96.6% in simulation and 93.1% in experiment, confirming the practicality and effectiveness of the proposed method for wireless AGV charging applications.

Acknowledgments

This research was supported by Electric Power University through project No. ĐTKHCN.06/2025.

References

[1] Z. Zhang, J. Chen, and Q. Guo, (2022) *"Application of Automated Guided Vehicles in Smart Automated Warehouse Systems: A Survey"* **Computer Modeling in Engineering and Sciences *134***(3): 1529–1563. DOI: 10.32604/cmes.2022.021451.

[2] D. Colling, J. Oehler, and K. Furmans, (2019) *"Battery Charging Strategies for AGV Systems"* **Logistics Journal: Proceedings** (15): DOI: 10.2195/lj_Proc_colling_en_201912_01.

[3] Q. S. Kabir and Y. Suzuki, (2018) *"Increasing Manufacturing Flexibility through Battery Management of Automated Guided Vehicles"* **Computers & Industrial Engineering *117***: 225–236. DOI: 10.1016/j.cie.2018.01.026.

[4] Y. Hao, J. Wang, and Y. Liu. "Research on Wireless Power Transfer System of Automated Guided Vehicle Based on Magnetic Coupling Resonance". In: *2019 22nd International Conference on Electrical Machines and Systems (ICEMS)*. 2019, 1–4. DOI: 10.1109/ICEMS.2019.8922021.

[5] H. Matsumoto, Y. Shibako, and Y. Neba, (2018) *"Contactless Power Transfer System for AGVs"* **IEEE Transactions on Industrial Electronics *65***(1): 251–260. DOI: 10.1109/TIE.2017.2721913.

[6] T.-S. Lee, S.-J. Huang, and M.-J. Wu, (2023) *"Enhancement of Wireless Power Transfer for Automated Guided Vehicles Considering Disturbance Suppression"* **IEEE Access *11***: 21508–21518. DOI: 10.1109/ACCESS.2023.3251890.

[7] C. Bharatiraja, A. Mahesh, and B. Lehman, (2025) *"Power Electronic Converters in Inductive Wireless Charging Applications for Electric Transportation"* **IEEE Journal of Emerging and Selected Topics in Power Electronics *13***(2): 2647–2683. DOI: 10.1109/JESTPE.2025.3526763.

[8] W. Li, C. C. Mi, S. Li, J. Deng, T. Kan, and H. Zhao, (2015) *"Integrated LCC Compensation Topology for Wireless Charger in Electric and Plug-in Electric Vehicles"* **IEEE Transactions on Industrial Electronics *62***(7): 4215–4225. DOI: 10.1109/TIE.2014.2384003.

[9] W. Li, H. Zhao, J. Deng, S. Li, and C. C. Mi, (2016) *"Comparison Study on SS and Double-Sided LCC Compensation Topologies for EV/PHEV Wireless Chargers"* **IEEE Transactions on Vehicular Technology *65***(6): 4429–2239. DOI: 10.1109/TVT.2015.2479938.

[10] M. Venkatesan, N. Rajamanickam, P. Vishnuram, M. Bajaj, V. Blazek, L. Prokop, and S. Misak, (2022) *"A Review of Compensation Topologies and Control Techniques of Bidirectional Wireless Power Transfer Systems for Electric Vehicle Applications"* **Energies *15***(20): 1–34. DOI: 10.3390/en15207816.

[11] C. Cheng, F. Lu, Z. Zhou, W. Li, Z. Deng, F. Li, and C. C. Mi, (2020) *"A Load-Independent LCC-Compensated Wireless Power Transfer System for Multiple Loads with a Compact Coupler Design"* **IEEE Transactions on Industrial Electronics *67***(6): 4507–4515. DOI: 10.1109/TIE.2019.2931260.

[12] J. Deng, B. Pang, W. Shi, and Z. Wang, (2017) *"Magnetic Integration of LCC Compensation Topology with Minimized Extra Coupling Effects for Wireless EV Charger"* **Energy Procedia *105***: 2281–2286. DOI: 10.1016/j.egypro.2017.03.659.

[13] F. Lu, H. Zhang, H. Hofmann, W. Su, and C. C. Mi, (2018) *"A Dual-Coupled LCC-Compensated IPT System With a Compact Magnetic Coupler"* **IEEE Transactions on Power Electronics *33***(7): 6391–6402. DOI: 10.1109/TPEL.2017.2748391.

[14] E. ElGhanam, M. Hassan, and A. Osman, (2021) *"Design of a High Power, LCC-Compensated, Dynamic, Wireless Electric Vehicle Charging System with Improved Misalignment Tolerance"* **Energies *14***(4): 885. DOI: 10.3390/en14040885.

[15] S. Li, W. Li, J. Deng, T. D. Nguyen, and C. C. Mi, (2015) *"A Double-Sided LCC Compensation Network and Its Tuning Method for Wireless Power Transfer"* **IEEE Transactions on Vehicular Technology *64***(6): 2261–2273. DOI: 10.1109/TVT.2014.2347006.

[16] H. Feng, T. Cai, S. Duan, J. Zhao, X. Zhang, and C. Chen, (2016) *"An LCC Compensated Resonant Converter Optimized for Robust Reaction to Large Coupling Variation in Dynamic Wireless Power Transfer"* **IEEE Transactions on Industrial Electronics *63***(10): 6591–6601. DOI: 10.1109/TIE.2016.2589922.

[17] H. R. Cha, R. Y. Kim, K. H. Park, and Y. J. Choi, (2019) *"Modeling and Control of Double-Sided LCC Compensation Topology with Semi-Bridgeless Active Rectifier for Inductive Power Transfer System"* **Energies *12***(20): 3921. DOI: 10.3390/en12203921.

[18] Y. Chen, J. Wu, H. Zhang, L. Guo, F. Lu, N. Jin, and D.-H. Kim, (2023) *"A Parameter Tuning Method for a Double-Sided Compensated IPT System With Constant-Voltage Output and Efficiency Optimization"* **IEEE Transactions on Power Electronics *38***(3): 4124–4139. DOI: 10.1109/TPEL.2022.3218709.

[19] Z. Yan, Y. Zhang, and Y. Liu, (2019) *"An LCC-P Compensated Wireless Power Transfer System with Constant Current Output and Reduced Receiver Size"* **Energies *12***(1): 172. DOI: 10.3390/en12010172.

[20] N. T. Diep, T. D. Hiep, and N. K. Trung, (2023) *"Constant Current Charging and Transfer Efficiency Improvements for a Dynamic Wireless Charging System"* **Engineering, Technology & Applied Science Research *13***(6): 12320–12326. DOI: 10.48084/etasr.6315.

[21] V.-B. Vu, D.-H. Tran, and W. Choi, (2018) *"Implementation of the Constant Current and Constant Voltage Charge of Inductive Power Transfer Systems with the Double-Sided LCC Compensation Topology for Electric Vehicle Battery Charge Applications"* **IEEE Transactions on Power Electronics *33***(9): 7398–7410. DOI: 10.1109/TPEL.2017.2766605.

[22] Z. Li, K. Song, J. Jiang, and C. Zhu, (2018) *"Constant Current Charging and Maximum Efficiency Tracking Control Scheme for Supercapacitor Wireless Charging"* **IEEE Transactions on Power Electronics *33***(10): 9088–9100. DOI: 10.1109/TPEL.2018.2793312.

[23] Z. Li, X. Huang, K. Song, J. Jiang, C. Zhu, and Z. Du. "Constant Current Charging and the Maximum System Efficiency Tracking for Wireless Charging Systems Employing Dual-side Control". In: *2018 International Power Electronics Conference (IPEC-Niigata 2018 - ECCE Asia)*. 2018, 84–87. DOI: 10.23919/IPEC.2018.8507468.

[24] K. Song, Z. Li, Z. Du, G. Wei, and C. Zhu. "Design for Constant Output Voltage and Current Controllability of Primary Side Controlled Wireless Power Transfer System". In: *2017 IEEE PELS Workshop on Emerging Technologies: Wireless Power Transfer (WoW)*. Chongqing, China, 2017, 1–6. DOI: 10.1109/WoW.2017.7959358.

[25] K. Song, Z. Li, J. Jiang, and C. Zhu, (2018) *"Constant Current/Voltage Charging Operation for Series-Series and Series-Parallel Compensated Wireless Power Transfer Systems Employing Primary-Side Controller"* **IEEE Transactions on Power Electronics *33***(9): 8065–8080. DOI: 10.1109/TPEL.2017.2767099.

[26] I.-W. Iam, C.-K. Choi, C.-S. Lam, P.-I. Mak, and R. P. Martins, (2024) *"A Constant-Power and Optimal-Transfer-Efficiency Wireless Inductive Power Transfer Converter for Battery Charger"* **IEEE Transactions on Industrial Electronics *71***(1): 450–461. DOI: 10.1109/TIE.2023.3241408.

[27] Z. Wang, H. Niu, K. He, X. Liu, and F. Gao. "Constant Power Control of LCC-LCC Compensated Wireless Charging Systems Based on Sensitivity Analysis". In: *2025 IEEE 16th International Symposium on Power Electronics for Distributed Generation Systems (PEDG)*. Nanjing, China, 2025, 286–290. DOI: 10.1109/PEDG62294.2025.11060185.